NeuroImage: Clinical 23 (2019) 101897

Contents lists available at ScienceDirect

NeuroImage: Clinical

journal homepage: www.elsevier.com/locate/ynicl

# Characterizing a perfusion-based periventricular small vessel region of interest

Sudipto Dolui[a], Dylan Tisdall[a], Marta Vidorreta[b,c], David R. Jacobs Jr[d], Ilya M. Nasrallah[a], R. Nick Bryan[e], David A. Wolk[b], John A. Detre[a,b,*]

[a] Department of Radiology, University of Pennsylvania, Philadelphia, PA, USA
[b] Department of Neurology, University of Pennsylvania, Philadelphia, PA, USA
[c] Siemens Healthcare S.L.U., Madrid, Spain
[d] Division of Epidemiology and Community Health, School of Public Health, University of Minnesota, Minneapolis, MN, USA
[e] Department of Diagnostic Medicine, University of Texas, Austin, Austin, TX, USA

ARTICLE INFO

*Keywords:*
Arterial spin labeling
Cerebral blood flow
Cerebral small vessel disease
Periventricular white matter
White matter lesions

ABSTRACT

The periventricular white matter (PVWM) is supplied by terminal distributions of small vessels and is particularly susceptible to developing white matter lesions (WML) associated with cerebral small vessel disease (CSVD). We obtained group-averaged cerebral blood flow (CBF) maps from Arterial Spin Labeled (ASL) perfusion MRI data obtained in 436 middle-aged (50.4 ± 3.5 years) subjects in the NHLBI CARDIA study and in 61 elderly (73.3 ± 6.9 years) cognitively normal subjects recruited from the Penn Alzheimer's Disease Center (ADC) and found that the lowest perfused brain voxels are located within the PVWM. We constructed a white matter periventricular small vessel (PSV) region of interest (ROI) by empirically thresholding the group averaged CARDIA CBF map at CBF < 15 ml/100 g/min. Thereafter we compared CBF in the PSV ROI and in the remaining white matter (RWM) with the location and volume of WML measured with Fluid Attenuated Inversion Recovery (FLAIR) MRI. WM CBF was lower within WML than outside WML voxels ($p < < 0.0001$) in both the PSV and RWM ROIs, however this difference was much smaller ($p < < 0.0001$) in the PSV ROI than in the RWM suggesting a more homogenous reduction of CBF in the PSV region. Normalized WML volumes were significantly higher in the PSV ROI than in the RWM and in the elderly cohort as compared to the middle-aged cohort ($p < < 0.0001$). Additionally, the PSV ROI showed a significantly ($p = .001$) greater increase in lesion volume than the RWM in the elderly ADC cohort than the younger CARDIA cohort. Considerable intersubject variability in PSV CBF observed in both study cohorts likely represents biological variability that may be predictive of future WML and/or cognitive decline. In conclusion, a data-driven PSV ROI defined by voxels with low perfusion in middle age defines a region with homogeneously reduced CBF that is particularly susceptible to progressive ischemic injury in elderly controls. PSV CBF may provide a mechanistically specific biomarker of CSVD.

## 1. Introduction

The brain is a metabolically-active organ, perfused by a disproportionate fraction of the cardiac output to supply its significant oxygen and nutrient requirements. While a partially redundant system of large arteries provides blood supply to the brain, its parenchyma is ultimately perfused by a dense network of microvessels (Moody et al., 1990).

Cerebral small vessel disease (CSVD) is thought to result from chronic and progressive pathologies affecting perforating cerebral arterioles and capillaries (Pantoni and Garcia, 1997; Prins and Scheltens, 2015), and is associated with typical vascular risk factors such as hypertension (de Leeuw et al., 2002; Liao et al., 1996; Verhaaren et al., 2013) and hyperlipidemia (Jimenez-Conde et al., 2010). Although CSVD can also be a mechanism of acute subcortical infarction, progressive small vessel dysfunction due to CSVD is considered to be the leading cause of vascular dementia (Pantoni, 2010).

White matter lesions (WMLs) detected as hyperintensities using Fluid Attenuated Inversion Recovery (FLAIR) magnetic resonance imaging (MRI), currently provide the most widely accepted biomarker of CSVD (Wardlaw et al., 2013). Several studies have demonstrated an

* Corresponding author at: Departments of Neurology and Radiology, University of Pennsylvania, 3W Gates Pavilion, 3400 Spruce Street, Philadelphia, PA 19104, Office: 517 Goddard Labs, USA.
*E-mail address:* detre@pennmedicine.upenn.edu (J.A. Detre).

https://doi.org/10.1016/j.nicl.2019.101897
Received 2 February 2019; Received in revised form 4 June 2019
Available online 12 June 2019

inverse relationship between the extent of WMLs and cognitive function (Gunning-Dixon and Raz, 2003; Marchant et al., 2012; Mayda et al., 2011). However, white matter lesions (WMLs) are not mechanistically specific for small vessel dysfunction and are observed in other pathologies such as multiple sclerosis and Alzheimer's disease (Kandel et al., 2016; Lee et al., 2016; McAleese et al., 2017). Even ischemic WMLs are not specific for CSVD, since WMLs may result from embolic mechanisms or hypoperfusion due to large artery disease (Caplan and Hennerici, 1998).

The periventricular white matter (PVWM) region is particularly susceptible to developing WMLs (Habes et al., 2016; Holland et al., 2008) likely because the PVWM is supplied exclusively by small vessels < 100 μ in diameter (Moody et al., 1990). PVWM lesions are very commonly observed in individuals aged 60 years or older (Habes et al., 2016; Kuo and Lipsitz, 2004; Longstreth Jr. et al., 1996), though with increasing severity they may become confluent with lesions in the deep white matter (DWM) (Fazekas et al., 1987; Kim et al., 2008).

The vascular anatomy of the PVWM and its susceptibility to developing WMLs suggest that it may be among the most weakly perfused regions in the human brain. Indeed, using single-photon emission computed tomography (SPECT) to measure group-averaged CBF map in 47 healthy middle-aged volunteers (age 34.3 ± 7.6 years), Holland et al. (2008) previously showed that cerebral blood flow (CBF) was reduced in the PVWM region compared to the remaining white matter, though that study relied on relative rather than absolute CBF mapping. A separate study by Sullivan et al. (O'Sullivan et al., 2002) used contrast-based perfusion MRI in a small cohort of patients with ischemic leukoaraiosis and controls and found that PVWM CBF was reduced in the patient group whereas GM and WM CBF did not differ.

In this study, we leveraged arterial spin labeled (ASL) perfusion MRI data from a large ($N$ = 436) middle-aged cohort in the Coronary Artery Risk Development in Young Adults (CARDIA) study to quantify regional CBF in human brain white matter. Although the sensitivity of ASL MRI for white matter CBF, particularly at the voxel level, has been controversial (van Gelderen et al., 2008), the advent of improved arterial spin labeling (Dai et al., 2008) and acquisition (Vidorreta et al., 2013) strategies has led to improved sensitivity for WM CBF (Zhang et al., 2016). By signal averaging ASL MRI data across N = 436 subjects, we were able to create a high quality CBF map capable of characterizing the spatial distribution of WM CBF. We aimed at i) confirming that the PVWM region is the most weakly perfused region of the human brain, corresponding also to the location of WMLs, and ii) demonstrating that the reduced CBF in PVWM is not attributable to partial volume effects from ventricles. We then constructed a data-driven region of interest (ROI) comprised of brain voxels showing sub-threshold CBF values and termed it the “periventricular small vessel” (PSV) ROI to indicate its periventricular location and sensitivity to small vessel disease based on the vascular anatomy of this region. Finally, in an independent separate local cohort of 61 cognitively normal older adults studied using a more sensitive background-suppressed 3D (BS-3D) ASL MRI methodology (Vidorreta et al., 2017a), we aimed to replicate i) and ii) and additionally to further characterize the PSV ROI by assessing if there is a differential relationship between CBF and WMLs in the PSV ROI as compared to the remaining white matter (RWM). Based on the findings of this study, we believe that CBF within the PSV ROI may provide a biomarker of small vessel function, and hence a mechanistically specific biomarker of CSVD.

## 2. Materials and methods

### 2.1. CARDIA MRI data

CARDIA is a multi-site, longitudinal study aimed at examining the development and determinants of clinical and subclinical cardiovascular disease. Using the same subsample as in our earlier study (Dolui et al., 2016b), MRI data from 436 healthy middle-aged subjects who underwent the CARDIA Year 25 MRI protocol on 3 Tesla Siemens MRI scanners in two acquisition sites, Minneapolis and Oakland, were included. The MRI protocols were approved by the Institutional Review Board of the University of Minnesota and the Kaiser Permanente Northern California (KPNC) Institutional Review Board for the two acquisition sites. All participants signed written informed consent for the brain MRI and for all other CARDIA procedures. The CARDIA data used in this study and all CARDIA data are available through the CARDIA Coordinating Center (http://www.cardia.dopm.uab.edu/contact-cardia) after approval of a paper proposal submitted to the CARDIA Publications and Presentations Committee.

The CARDIA MRI protocol included:

i) Non-background suppressed 2D pseudocontinuous ASL (pCASL) data acquired using a custom sequence (Chen et al., 2011) based on gradient-echo echoplanar imaging (EPI) with TR/TE = 4000/11 ms, voxel size = 3.4 × 3.4 × 5 $mm^3$, matrix = 64 × 64, flip angle = 90°, FOV = 220 × 220 $mm^2$, GRAPPA = 2, bandwidth = 3004 Hz/pixel, echo spacing = 0.44 ms and EPI factor = 64. 20 slices with a distance factor of 20% were acquired from inferior to superior in a sequential order. The labeling was performed with a labeling duration of 1.48 s, post labeling delay (PLD) = 1.5 s (range: 1.50–2.17 s for the inferior to the superior slices) at 9 cm below the center of the imaging volume. 40 label/control pairs were acquired for signal averaging.
ii) Sagittal T1-weighted 3D magnetization-prepared rapid gradient echo (MPRAGE) data acquired with TR/TE/TI = 1900/2.9/900 ms, flip angle = $9^0$, bandwidth = 170 Hz/pixel, voxel size = 1x1x1 $mm^3$, matrix = 256 × 256, slices = 176, GRAPPA = 2.
iii) Sagittal 3D FLAIR data acquired with TR/TE/TI = 6000/160/2200 ms, voxel size = 1x1x1 $mm^3$, 160 slices, matrix = 256 × 220, bandwidth = 930 Hz/px, GRAPPA = 2.

### 2.2. Penn Alzheimer's Disease Center MRI data

We also considered MRI data from 61 cognitively intact elderly subjects obtained from the Penn Alzheimer's Disease Center (ADC) Clinical Core as part of a longitudinal cohort study of aging and Alzheimer's Disease. All Penn ADC subjects receive annual clinical and cognitive assessment and their clinical status was decided at a consensus meeting attended by neurologists, psychiatrists, radiologists and neuropsychologists based on medical and neurological examinations, psychometric assessments and imaging (Dolui et al., 2017; Xie et al., 2016). The MRI protocols were approved by the Institutional Review Board of the University of Pennsylvania and written consent was obtained from all the subjects.

Multimodal MRI was performed on a Siemens Prisma 3 Tesla whole body scanner using a 32-channel head coil. The Penn ADC protocol included:

i) Background-suppressed ASL MRI acquired with an unbalanced pCASL technique using a custom 1D-accelerated 4-shot 3D spiral acquisition (Vidorreta et al., 2017a) with TR = 4.25 s, TEeff = 9.78 ms, 90% background suppression, an isotropic voxel resolution of 2.5 $mm^3$, matrix = 96 × 96, flip angle = $90^0$, FOV = 240 × 240 $mm^2$, bandwidth = 400 Hz/px. The labeling was obtained with 1.8 s labeling and 1.8 s PLD with an unbalanced pCASL, which provides optimal labeling efficiency in the presence of off-resonance effects at the labeling plane (Zhao et al., 2017). The labeling plane was placed at an optimal location perpendicular to straight segments of the carotid and vertebral arteries based on time-of-flight angiography to maximize labeling efficiency (Vidorreta et al., 2017b). Two M0 images with TR = 6 s and without background suppression and pCASL labeling were acquired and averaged to be used for CBF quantification. Ten label/control pairs were acquired for averaging.

**Table 1**
Demographics of the two cohorts.

| Demographics | CARDIA | ADC |
|---|---|---|
| Age (years) | 50.4 ± 3.5 (range: 43–56) | 73.2 ± 6.9 years (range: 59–88) |
| Sex (% Female) | 54 | 63 |
| Hypertensive[a] (% subjects) | 26.4% | 44.3% |
| Type 2 Diabetes (% subjects) | 7.1% | 19.7% |
| Cardiac or cerebrovascular events (% subjects) | 1.4% | 19.7% |
| Current and former smokers (% subjects) | 39.5% | 63.6% |

[a] Hypertensive defined by blood pressure higher than 140/90 mmHg or taking medication in the CARDIA cohort and by patient/informant report of history of hypertension or through review of the medical record in the ADC cohort.

ii) High-resolution sagittally acquired T1 images collected using 3D MPRAGE with the following parameters: TR/TE/TI = 2400/2.24/1000 ms, flip angle = $8^0$, bandwidth = 210 Hz/px, voxel size = 0.8 × 0.8 × 0.8mm$^3$, matrix = 300 × 320, slices = 208, GRAPPA = 2.
iii) FLAIR data obtained with TR/TE/TI = 6000/289/2200 ms, voxel size = 1x1x1 mm$^3$, matrix = 256 × 220, 160 slices, bandwidth = 930 Hz/px, GRAPPA = 2.

Demographic information for the 436 middle-aged subjects from the CARDIA cohort and 61 cognitively normal elderly subjects from the Penn cohort are provided in Table 1.

### 2.3. Data processing

All data were processed using an in-house pipeline implemented in MATLAB with SPM12 and FSL (Jenkinson et al., 2012).

The T1 images were probabilistically segmented into gray matter (GM), white matter (WM) and cerebrospinal fluid (CSF) using the SPM12 segmentation tool. The resulting segmentations were subsequently used to compute a brain mask containing GM, WM and ventricular CSF. Each subject's T1-weighted images were also used to estimate a subject-specific non-linear warping to the MNI152 template using FMRIB's non-linear image registration tool (FNIRT) (Andersson et al., 2010).

ASL processing steps consisted of first realigning the raw EPI (or stack-of-spirals for the ADC cohort) images using the method by Wang (2012). The mean EPI image, obtained by temporally averaging the realigned EPI time series, was coregistered to the structural image using FSL boundary based registration (BBR). In the case of the ADC cohort, the M0 image was first coregistered to the mean stack-of-spirals images using SPM with a normalized mutual information criterion and thereafter this coregistered M0 image was coregistered to the T1 image using FSL BBR. Note that our background suppression is only 90% leading to enough remaining contrast between the tissue types in the stack-of-spirals images for registration. Pairwise subtraction of the label-control images was performed and the difference was converted to absolute CBF time series measurements using a single compartment model (Alsop et al., 2015) with parameters: brain/blood partition coefficient = 0.9, $T_{1,blood}$ = 1.664 s, Labeling efficiency = 0.85 for CARDIA and 0.72 (Vidorreta et al., 2013) for ADC data. Reduced labeling efficiency in the 3D BS acquisition reflects spoiling of some label by the two background suppression pulses. Additionally, for CARDIA data, a denoised mean CBF map was obtained from the CBF time series by discarding outlier volumes based on a structural correlation criterion (Dolui et al., 2016a) followed by a voxelwise processing using a robust Bayesian approach (combined method referred to as "SCRUB") (Dolui et al., 2016c). We did not apply SCRUB post-processing to the ADC data because of the limited number of label-control pairs and higher temporal signal to noise ratio (TSNR) in background suppressed 3D acquisition (Vidorreta et al., 2013). Each subjects' CBF map was normalized to the MNI152 space using a subject specific ASL-to-MNI152 warp obtained by concatenating the ASL-to-T1 BBR coregistration parameters with T1-to-MNI152 warp with a tri-linear interpolation.

White matter lesions were segmented using FLAIR images by the lesion growth algorithm (LGA) (Schmidt et al., 2012) as implemented in the Lesion segmentation toolbox (LST) (www.statistical-modelling.de/lst.html). The LGA algorithm accepts a FLAIR and a T1 image and outputs a lesion probability for each voxel (henceforth we will refer it as LST lesion probability) in the T1 space. The LST lesion probability maps were warped to the MNI152 space using T1-to-MNI152 warp and tri-linear interpolation.

### 2.4. Periventricular small vessel (PSV) region of interest (ROI)

To define a region of interest (ROI) representing weakly perfused brain voxels, we considered the CARDIA group-averaged CBF map, symmetrized bilaterally and thresholded to CBF < 15 ml/100 g/min, a threshold previously shown to potentially predict future occurrence of ischemic lesions based on dynamic susceptibility contrast perfusion MRI (Bernbaum et al., 2015). We further modified the ROI to remove the ventricles using a white matter mask in the MNI152 space obtained by i) warping each subjects white matter probabilistic segmentation to the MNI space, ii) averaging the maps across the cohort and iii) thresholding it to 5%. Note that although 5% is a liberal threshold, we also modified this ROI in all the subsequent analyses as detailed below in section 2.5. Some regions in cerebellum and brain stem also showed group-averaged CBF < 15 ml/100 g/min, likely representing artifact at the edges of the imaging volume, and were removed manually. The resulting PSV ROI is shown in Fig. 3 (see Results). Note that this ROI is in the MNI space and was same for all subjects in both cohorts. An MNI space RWM was constructed by subtracting the PSV ROI from a WM mask computed by thresholding the CARDIA group-averaged WM tissue probability map to 0.5 (also shown in Fig. 3).

Subject-specific PSV ROIs were then constructed by warping the MNI152-space ROI back to each subject's space with the inverse FNIRT transformation and were further refined by intersecting the warped map with a WM ROI (obtained by smoothing the subject's WM tissue probability map with an isotropic Gaussian kernel with FWHM = 5 mm and binarized with a threshold of 0.5). We also constructed subject-specific remaining white matter (RWM) ROIs comprised of the WM ROIs outside the PSV ROIs.

### 2.5. Analytical and statistical methods

We aimed to assess the CBF distribution in white matter and determine if there was a differential relationship between CBF and LST-derived WML volume in the PSV ROI as compared to the RWM.

#### 2.5.1. Group averaged CBF map and lesion frequency map and their distribution

To obtain the spatial distribution of CBF and WML in each cohort, the MNI152-space CBF and LST lesion probability maps were averaged across subjects at each voxel to produce subject-averaged maps for each cohort. Note that averaging the LST lesion probability maps across subjects provides a measure of lesion frequency of each voxel since it shows the fraction of subjects in the cohort having lesion in that voxel. These maps were visualized for qualitative comparison.

#### 2.5.2. Assess effects of partial volume contamination on observed CBF distribution

To demonstrate that observed WM CBF distributions in group data were not the result of partial volume effects across tissue types with differing CBF values, we constructed pseudo-CBF maps for each subject by i) smoothing the anatomical tissue probability maps to account for

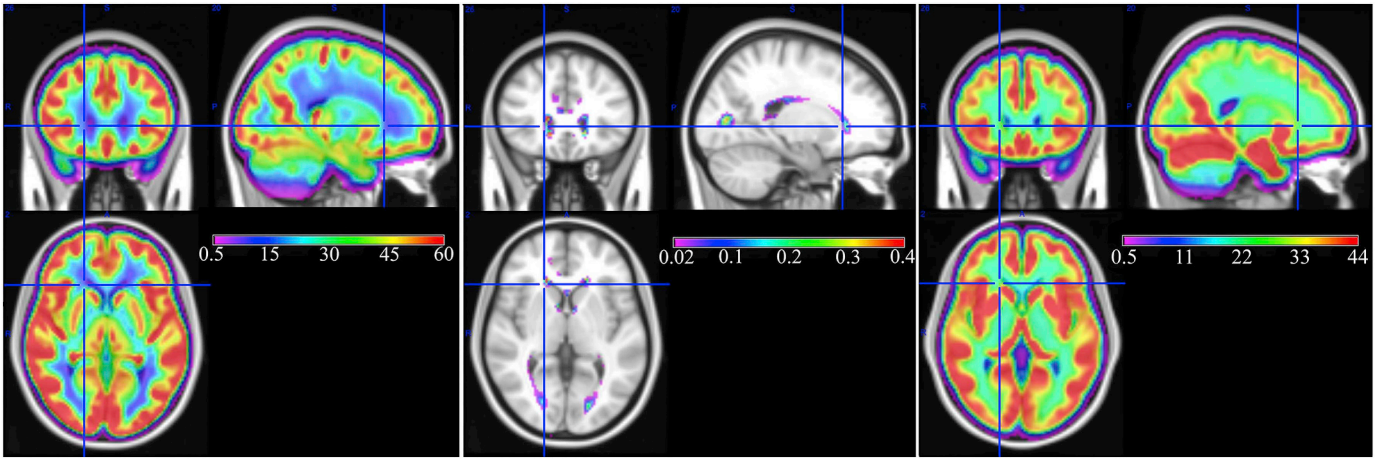


**Fig. 1.** Group averaged maps in the CARDIA cohort. (Left) Group averaged CBF, (Middle) Group averaged white matter lesion frequency, and (Right) Group averaged structural pseudo-CBF computed as weighted average of tissue probability maps (note the absence of a periventricular CBF gradient in the pseudo-CBF map). Gray matter CBF appears red and yellow while white matter CBF appears green and blue. (For interpretation of the references to color in this figure legend, the reader is referred to the web version of this article.)

the inherent point spread function (PSF) of ASL and downsampling them to the ASL space, and ii) constructing a weighted average of the tissue probability maps where the weights in the GM and WM were equal to the mean CBF in the respective tissues derived from ASL MRI data and zero in CSF. The pseudo-CBF maps were then warped to the MNI152 template space and were averaged across subjects. To estimate the PSF of both 2D EPI and 3D RARE stack-of-spirals readouts, we simulated the time evolution of the vascular signal for each case. This allowed us to obtain the modulation transfer function (MTF) of the CBF signal along all directions. For each direction, the PSF was computed as the Fourier transform of the MTF, and we computed its Full-Width Half-Max (FWHM) as estimator of the spatial smoothing along that direction leading to the smoothing kernels with FWHM = [0, 3.5, 0] mm for the 2D and [3.1, 3.1, 3.2] mm for the 4 shot 3D data.

Pearson's correlation coefficients were used to calculate the voxel-wise correlations between the group averaged CBF map and the pseudo-CBF map, in both the PSV and RWM ROIs in each cohort. These correlation coefficients were calculated to provide a metric of the extent of spatial similarity. Recognizing that there is spatial autocorrelation between neighboring voxels resulting in overestimation of degrees of freedom and spuriously low *p*-values, this analysis focuses just on the correlation values, rather than on their statistical significance.

#### 2.5.3. Relationship between CBF inside and outside WMLs in PSV ROI versus RWM

To determine if CBF differs within and outside WMLs and if this difference varies across the PSV and RWM ROIs, we used a two-way repeated measures ANOVA with the two factors being ROI (PSV and RWM) and lesion-location (inside or outside lesion). For this, we upsampled the CBF maps to the T1 space and extracted median CBF values from four ROIs; PSV versus RWM and inside versus outside lesions. Subject specific PSV and RWM ROIs were constructed as described above and the regions outside and inside lesions were defined by zero and non-zero LST lesion probabilities (lesionprob), respectively. This analysis focuses primarily on the ADC data because the constructed PSV ROI was fully independent of that cohort. We also reported the results with the CARDIA data while noting that the PSV ROI was defined by its voxels having the lowest CBF values in the brain, though not by the presence of lesions.

#### 2.5.4. Normalized lesion volumes in PSV and RWM

Normalized lesion volumes (i.e. lesion volume normalized to the ROI volume) within PSV and RWM were computed by averaging the LST lesion probabilities within the ROIs in the subject-T1-space (method of constructing the ROIs for each subject was described above) and were compared across the two cohorts to determine if any region is more susceptible to develop lesion with age. A two-way mixed ANOVA with the within-subject factor of ROI (PSV or RWM) and the between-subject factor of group cohort (CARDIA or ADC) was used for the analysis. The statistical tests were obtained after log-transformation of the normalized lesion volumes because of the skewed nature of the data (positive skew).

#### 2.5.5. Comparison of PSV CBF in the two cohorts

For both CARDIA and Penn ADC cohorts, we report the mean CBF within the PSV ROI and compare their mean and variances using two sample *t*-test and F test for equality of variances respectively. Comparison of mean was performed to assess change in PSV CBF across age range while comparison of variance was expected to provide the variability in the two age ranges.

#### 2.5.6. Comparison of sensitivities between the two ASL methods

Finally, we report the mean temporal signal to noise ratio (TSNR) for the PSV ROI data, which illustrates the differences in sensitivity between the two ASL MRI methodologies employed. TSNR is related to the feasibility of measuring CBF. An acquisition with low TSNR will require signal averaging of larger number of volumes to obtain a reliable estimate. Note that the TSNR calculated here is for the CBF time series and not for the raw EPI or stack-of-spirals time series. To compute TSNR for each ROI, mean CBF within the ROI was computed for each CBF volume of the time series, and the TSNR was computed as the ratio of the mean and standard deviation of the values. For comparison with published ASL TSNR values, we also report the TSNR in gray matter for both datasets.

A schematic diagram of the construction of the ROI and its use in the different analyses is provided in the supplementary material.

## 3. Results

### 3.1. Group averaged CBF map and lesion frequency map and their distribution

The left and middle subplots of Fig. 1 show the group averaged CBF map and lesion frequency map from the middle-aged CARDIA cohort. The group averaged CBF map demonstrates that WM CBF is specifically decreased in the periventricular region (blue voxels in Fig. 1, left). The analogous map for the ADC cohort is shown in the left subplot of Fig. 2. As expected, CBF was generally lower in the elderly cohort (note the

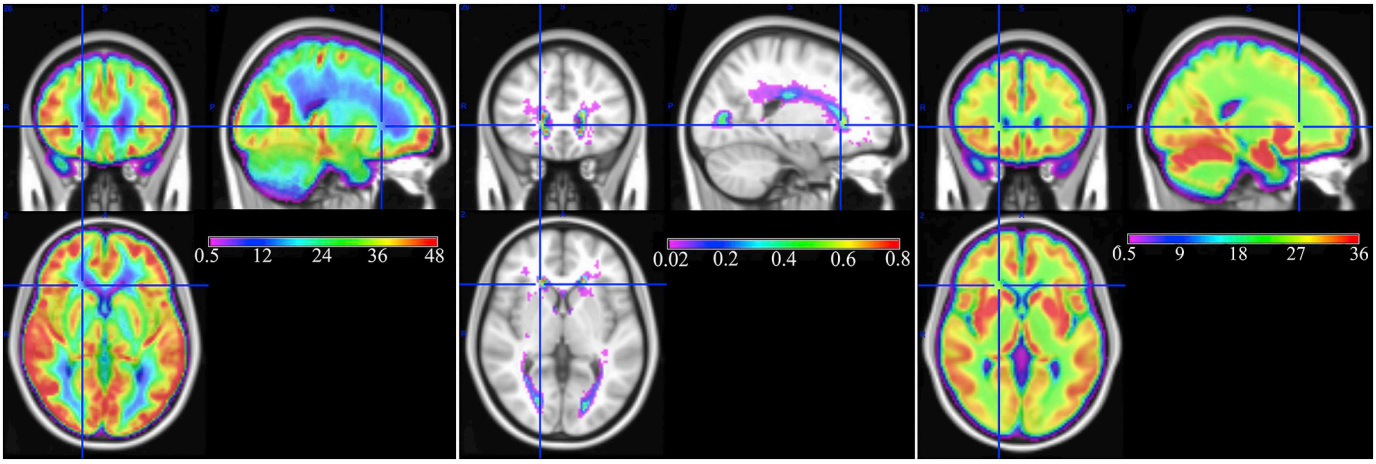


**Fig. 2.** Group averaged maps in the Penn ADC cohort. (Left) Group averaged CBF, (Middle) Group averaged white matter lesion frequency and (Right) Group averaged structural pseudo-CBF computed as weighted average of tissue probability maps. Gray matter CBF appears red and yellow while white matter CBF appears green and blue. Note that the colorscale differs from that used for the CARDIA data to better visualize the lower CBF values and higher lesion frequency in this elderly cohort. (For interpretation of the references to color in this figure legend, the reader is referred to the web version of this article.)

differences in color scales in Figs. 1 and 2). However, in both cohorts, CBF was lowest in the periventricular region with a largely consistent spatial pattern.

The middle subplot of Fig. 1 shows the group averaged lesion frequency in the CARDIA cohort. The lesion frequency is shown only for regions where the frequency is above 2%, i.e. 2 out of 100 subjects showed a lesion, on average. It demonstrates that, although lesion frequency is low in this middle-aged cohort, lesions are most frequent in the periventricular region where group averaged CBF is lowest. The analogous map for the ADC cohort shown in the middle subplot of Fig. 2 demonstrates similar results with the highest lesion frequency seen in the periventricular region. The spatial extent of suprathreshold lesion voxels in the elderly ADC cohort was much larger than for the younger CARDIA sample.

Fig. 3 shows the ROI comprised of hypoperfused voxels generated from the CARDIA cohort data as described in the Methods (red voxels). As expected from Fig. 1, the resulting ROI is located within the PVWM region, and is therefore referred to as the “periventricular small vessel” (PSV) ROI because this region is also perfused by the terminal distributions of small penetrating arteries. An ROI comprised of the remaining WM (RWM ROI) was also generated (blue voxels in Fig. 3).

### 3.2. Assess effects of partial volume contamination on observed CBF distribution

The right subplot of Fig. 1 shows the subject-averaged pseudo-CBF map for the CARDIA cohort. This map did not show a CBF gradient in the PSV region as was present in the true CBF map (compare Left and Right images) suggesting that the observed periventricular CBF reductions are not attributable to partial volume effects. The pseudo-CBF map for the ADC cohort (Fig. 2) recapitulates the results from the CARDIA data. Taking each voxel in the group-average maps as having both a CBF and pseudo-CBF score, we performed Pearson's correlation tests on these values. For the middle-aged CARDIA cohort, the correlation between CBF and pseudo-CBF was 0.76 in RWM and 0.21 in PSV ROI, demonstrating that CBF in the PSV is much more poorly explained by the underlying anatomy than that in RWM. Very similar results were seen in the elderly Penn ADC cohort where the voxel-wise correlation between the two maps was 0.58 in the RWM and 0.22 in the PSV ROI.

### 3.3. Lesional and non-lesional CBF values

We performed repeated measures ANOVAs for the ADC cohort on absolute CBF values, subdividing the PSV and RWM ROIs into two further sub-categories according to the presence or absence of lesions (lesionprob = 0 or lesionprob > 0), where lesionprob refers to LST

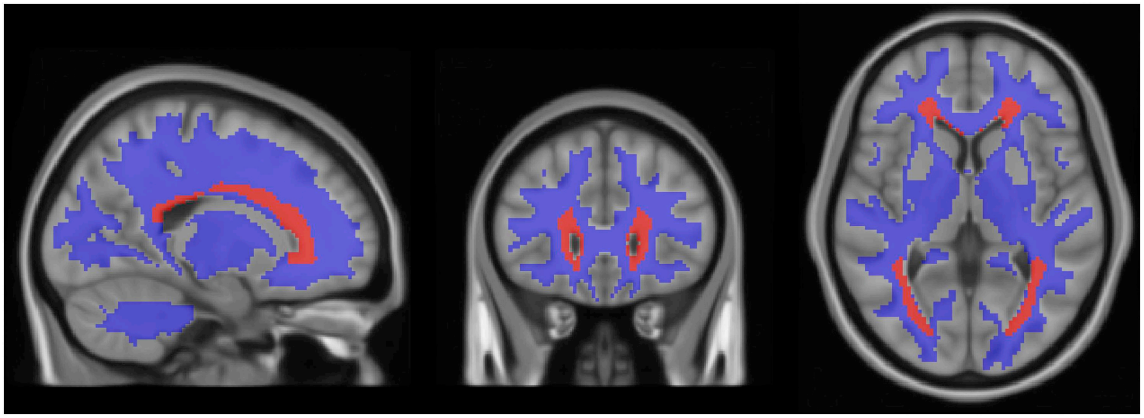

**Fig. 3.** Periventicular small vessel (PSV) ROI (shown in red) and the remaining white matter (shown in blue) overlaid on MNI152 template. The PSV ROI was obtained by thresholding the group-averaged and bilaterally symmetrized CARDIA CBF map to 15 ml/100 g/min and manually removing artifactual regions in cerebellum and brainstem. (For interpretation of the references to color in this figure legend, the reader is referred to the web version of this article.)

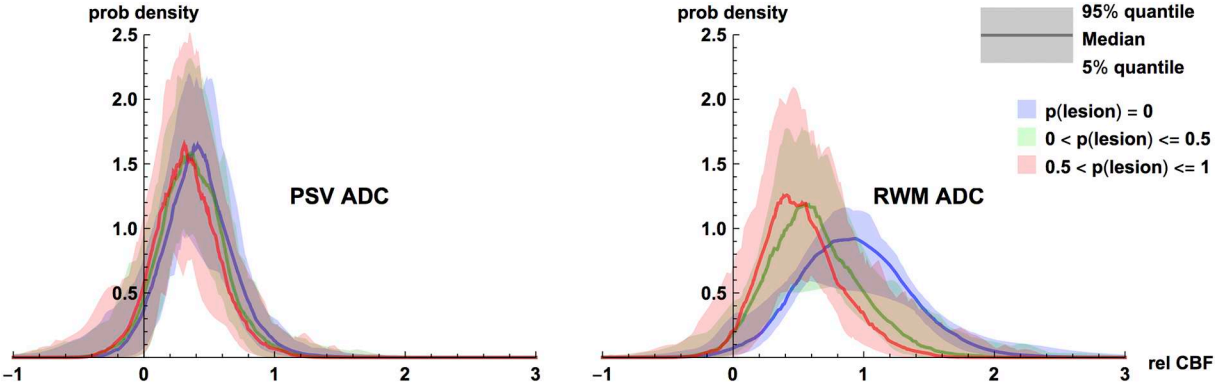


**Fig. 4.** Plots of empirical probability density functions (PDFs) of relative CBF in (Left) the Periventricular Small Vessel (PSV) and (Right) the remaining white matter (RWM) with the ADC ASL data. Within each category, PDFs are separately plotted for voxels with lesionprob = 0, 0 < lesionprob ≤ 0.5, and 0.5 < lesionprob ≤ 1 (see colors in legend). Empirical PDFs were computed for each subject separately and we have plotted the across-subject median PDF value (solid lines) and the across-subject 5%–95% quantile region (colored regions) for each relative CBF. (For interpretation of the references to color in this figure legend, the reader is referred to the web version of this article.)

lesion probability. As expected, mean CBF inside lesions was lower than that outside lesions ($p < < 0.0001$, partial $\eta^2 = 0.75$) and in the PSV compared to RWM ($p < < 0.0001$, partial $\eta^2 = 0.93$). Further, there was a statistically significant ($p < < 0.0001$, partial $\eta^2 = 0.73$) interaction between the two factors showing that the difference between CBF inside and outside lesions was significantly higher in the RWM as compared to the PSV. Fig. 4 illustrates this CBF/lesion relationship by binning voxel-wise CBF and LST lesion probabilities into three groups: (lesionprob = 0, 0 < lesionprob ≤ 0.5 and 0.5 < lesionprob ≤ 1. To remove inter-subject variability unrelated to the within-subject CBF/lesion relationship, we normalized each subject's voxel-wise CBF values against their whole-brain mean CBF, producing relative CBF values (relCBF). We then computed empirical probability density functions (PDFs) p(relCBF | lesion group = g, PSV) and p(relCBF | lesion group = g, RWM). The shapes of the subject-median PDFs are plotted, and their between-subject variability is shown by the shaded region (at each value of relCBF, the density function for the 5% and 95% percentile subject is shaded). Inspecting this figure, we can see that relCBF in regions with no lesion (lesionprob = 0) is higher than that with low (0 < lesionprob ≤ 0.5) and high (0.5 < lesionprob ≤ 1) lesion probabilities. However, the difference is more apparent in the RWM, while in the PSV ROI, there is considerable overlap.

CARDIA data also showed similar results, with CBF inside lesions lower than outside lesion ($p < < 0.0001$, partial $\eta^2 = 0.59$), CBF in the PSV ROI lower than in the RWM ($p < < 0.0001$, partial $\eta^2 = 0.89$), and an interaction between the two terms ($p < < 0.0001$, partial $\eta^2 = 0.34$). Note that the result that CBF in the PSV ROI is lower than that in the RWM was preselected in the CARDIA data because the PSV ROI was defined by its low CBF.

### 3.4. Normalized lesion volumes in PSV and RWM

The normalized lesion volumes, defined as total lesion volume per unit ROI volume, and expressed as median (interquartile range) percent, were found to be 1.28 (1.53) and 4.90 (7.43) in the PSV ROI in the CARDIA and ADC cohorts, respectively, and 0.16 (0.15) and 0.51 (0.73), respectively, in the remaining white matter (RWM). The normalized lesion volumes were 8.7 (6.6) times higher in the PSV ROI than in RWM in the middle-aged subjects, increasing to 10.8 (6.5) times higher in the elderly subjects. A mixed ANOVA with ROI (RWM and PSV) as within-subject factor and age/cohort (middle-aged CARDIA and elderly ADC) as between-subject factor demonstrated that normalized lesion volumes were significantly higher ($p < < 0.0001$, partial $\eta^2 = 0.84$) in the PSV than RWM ROI, and in the elderly ADC cohort as compared to the CARDIA cohort ($p < < 0.0001$, partial $\eta^2 = 0.21$). Moreover, there was a statistically significant ($p = .001$, partial $\eta^2 = 0.022$) interaction of age and ROI with the elderly cohort demonstrating a greater increase in normalized lesion volume in the PSV ROI than in the RWM.

### 3.5. Comparison of PSV CBF in the two cohorts

The average PSV CBF for the CARDIA and the ADC cohort were 12.99 ± 5.52 and 12.29 ± 4.66 ml/100 g/min respectively. The between cohort difference in PSV CBF was not significant ($p = .34$) and there was a weak trend ($p = .11$) of higher variance in the CARDIA cohort compared to the ADC cohort.

### 3.6. Comparison of sensitivities between the two ASL methods

The TSNR (reported as median (interquartile range) because of its right skewed distribution) in the PSV ROI for the CARDIA cohort was 0.34 (0.27), which was about 12.5 times lower than in the ADC cohort with TSNR value of 4.25 (3.36). In both cohorts, TSNR values in the gray matter were significantly higher than in the PSV, with values of 3.82 (2.43) and 11.27 (6.71) in the CARDIA and ADC data, respectively.

## 4. Discussion

We defined a periventricular small vessel region of interest (PSV ROI) reflecting a brain region supplied by small vessels where we observed reduced perfusion in a large middle-aged cohort. CBF in this ROI is proposed as a measure of small vessel functional integrity and a potential biomarker of small vessel disease. By averaging across a large number of subjects, the spatial distribution of WM CBF was assessed in both the large CARDIA cohort as well as the smaller ADC cohort in whom a more sensitive ASL MRI acquisition was available. The observed WM CBF distribution was found to be highly non-uniform in both cohorts, showing morphologically comparable extended region of reduced perfusion in the periventricular regions. Similar CBF gradients have previously been observed in group averaged CBF maps obtained with Positron Emission Tomography (PET) and SPECT data (Henriksen et al., 2018; Holland et al., 2008; Ito et al., 2006), albeit with lower resolution. In both cohorts, FLAIR WMLs were also found to coincide with the most poorly perfused regions and the observed spatial distribution of the lowest CBF values also matches WML frequency maps derived from other cohorts (DeCarli et al., 2005; Habes et al., 2016; Holland et al., 2008; Rostrup et al., 2012; Yoshita et al., 2006). While the causality of low CBF and occurrence of lesions cannot be discerned from cross-sectional data, the PSV ROI was of larger extent than the

regions of highest WML frequency, suggesting a penumbral region susceptible to future ischemic injury.

Periventricular localization has previously been described in the context of WMLs, which have been categorized as periventricular when their location was morphologically adjacent to the ventricles (De Groot et al., 2002; ten Dam et al., 2007). Note, however, that this type of categorization is difficult or impossible to obtain when the periventricular and deep white matter lesions become confluent. Popular visual rating scales such as the Fazekas (Fazekas et al., 1987) or Scheltens (Scheltens et al., 1993) scales have also been used to categorize the lesions into periventricular and deep white matter, along with their severity including confluence between the regions, though disagreement between rating scales has contributed to inconsistent conclusions across studies (Mantyla et al., 1997). Subject specific periventricular ROIs have also been constructed through automated dilation of the segmented ventricles by 5–10 mm (Bahrani et al., 2017; DeCarli et al., 2005; Ghaznawi et al., 2018; Griffanti et al., 2018). In contrast, the PSV ROI in the current study was defined exclusively based on a CBF threshold rather than ventricular anatomy. The ROI is highly non-isotropic around the ventricles with higher extent in the caps of the lateral ventricles. A highly conserved pattern of reduced CBF was present in the CBF distributions of both middle aged and elderly cohorts, indicating that the perfusion-based definition is consistent.

The group-averaged pseudo-CBF maps did not demonstrate an appreciable PSV CBF gradient, as was observed in actual group CBF maps. This was further verified by comparing the correlations between CBF and pseudo-CBF obtained from the RWM and PSV ROI. Although correlations between actual and pseudo-CBF were quite high in both the cohorts for the RWM, this correlation was considerably reduced in the PSV region, demonstrating that tissue classifications of WM/GM/CSF alone are not sufficient to describe the observed spatial variations in CBF in PSV region. As the structural tissue segmentations were smoothed to account for the point spread function of the ASL acquisition and downsampled to the resolution of ASL before warping to the MNI152 space, reductions of CBF observed in the PSV region are highly unlikely to simply reflect partial volume effects. Notably any other potential source of blurring would not be expected to uniquely affect the PSV region, which is not isotropically distributed around the ventricles. Accordingly, hypoperfusion in the PSV region also does not reflect limitations of spatial resolution in ASL MRI.

A distinct difference between the effects of lesions on CBF in PSV versus RWM was observed, as illustrated in Fig. 4, and was analytically verified from the repeated measures ANOVA with the ADC data. While CBF declines with increases in LST lesion probability in both regions, the magnitude of this effect was much larger in RWM than in PSV. In contrast, in the PSV region, CBF distributions are more similar across lesion probabilities, suggesting that CBF decreases more uniformly in the PSV than in the RWM. In other words, low CBF in the PSV ROI is not exclusively the result of measuring CBF within lesions. The repeated measures ANOVA also showed significantly higher CBF in the RWM compared to the PSV. The results with the CARDIA data were similar. For these analyses, we categorized voxels as lesions based on non-zero LST lesion probability in this study, but the results were very similar with a threshold of 0.5.

Normalized white matter lesion volumes were found to be higher in the PSV region compared to the RWM in both study cohorts. Interestingly the difference was significantly higher in the elderly cohort suggesting that the PSV ROI is more susceptible to demonstrate lesions with increasing age than RWM, lending the proposed ROI some preliminary pathophysiological significance. Note that the PSV ROI used for this analysis was defined purely based on hypoperfusion in the middle-aged cohort, yet still showed increased normalized lesion volume in the elderly cohort. These findings are consistent with the notion that PSV lesions are likely ischemic in etiology (Fernando et al., 2006), potentially reflecting the cumulative effects of reduced CBF over many years, though confirmation in longitudinal data is needed to evaluate this.

Although CBF was generally lower in the elderly ADC cohort than in the middle-aged CARDIA cohort, mean CBF in the PSV ROI of the middle-aged CARDIA cohort was not significantly higher than the elderly ADC cohort. This may reflect underestimation of PSV CBF in the CARDIA cohort due to use of a shorter postlabeling delay (see technical limitations, below) and/or increased partial volume contamination from CSF due to larger voxel size in the CARDIA ASL data. There was also a weak trend of higher intersubject variability of PSV CBF in the CARDIA cohort than in the ADC cohort, likely reflecting differences in measurement noise across ASL acquisition methodologies, though both cohorts showed considerable variability. The finding that between-subject variability was not substantially smaller in the ADC data, despite having a TSNR 12 times higher than the CARDIA cohort, suggests that at least some of the between-subject variability in both cohorts is biological. This biological variability in PSV CBF may ultimately provide explanatory power to predict the future development of WML or cognitive deficits associated with CSVD.

The relationship between cerebral blood flow (CBF) and WMLs has been studied before. Specifically, global and regional gray matter (GM) and white matter (WM) CBF were found to be lower in subjects with more WMLs (Bisschops et al., 2004; Shi et al., 2016; Vernooij et al., 2008). Additionally, CBF was found to be lower inside the lesions (Brickman et al., 2009; van Dalen et al., 2016), and also in lesion penumbras (Promjunyakul et al., 2015). Longitudinal studies comparing the chronological order of occurrence of lesion and hypoperfusion however showed mixed results with WMLs predating decreasing CBF (van der Veen et al., 2015), and the reverse (Promjunyakul et al., 2015; Promjunyakul et al., 2018; ten Dam et al., 2007). Ten Dam et al. (2007) specifically showed increases in periventricular lesions in subjects with low global CBF. Additionally Promjunyakul et al. (2018) showed low baseline CBF in regions of future occurrence of lesions in the PVWM region, but not in the deep white matter region, at an average interscan interval of 17 months. The current study, although not longitudinal, had the advantage of a much larger sample size compared to most of the previous studies, higher spatial resolution than studies using CBF quantification with PET or SPECT (Holland et al., 2008), and better labeling (PCASL) and acquisition (BS-3D) strategies coupled with advanced data cleaning procedures than the studies using PASL (Promjunyakul et al., 2015; Promjunyakul et al., 2018; Promjunyakul et al., 2016).

The study has a few technical limitations. First, data from both the cohorts were obtained with single post labeling delay (PLD; the time interval between labeling and image acquisition to allow the labeled blood to enter the microvasculature). A PLD shorter than the arterial transit time (ATT; the time taken by the tagged blood to reach the imaging voxel from the labeling location) leads to underestimation of CBF due to incomplete delivery of the labeled blood during imaging. CARDIA used a PLD of 1.5 s, however the slices were obtained with 2D acquisitions from inferior to superior direction with the last slice acquired approximately 670 ms after the initial PLD. Thus, the effective PLD in the superior slices was much longer than the nominal value, with the mean PLD across the brain being approximately 1.84 s. ADC scans were obtained with a PLD of 1.8 s. Hence the PLDs were close to the arterial transit time of WM, whose reported values range from 1.5 s (Wu et al., 2013) to 1.7 s (Zhang et al., 2016). Furthermore, continuous ASL methods such as pCASL label a temporal bolus of arterial blood, so these are the minimum PLD's for the end of the ASL bolus, with the start of the ASL bolus having a 1.5 s longer PLD for the CARDIA data and 1.8 s longer PLD for the ADC data. However, since no prior studies have specifically measured ATT in the PSV ROI, it is possible that this region has a longer ATT than other WM regions, which would lead to underestimation of CBF. For example, if ATT = 2 s instead of 1.8 s, it would lead to an approximately 15% underestimation of CBF based on simulation (Buxton et al., 1998). Nevertheless, a 15% increase in CBF for regions with CBF $<$ 15 ml/100 g/min would have still been considered hypoperfused compared to the RWM.

Second, while CARDIA used the currently recommended pCASL labeling approach (Alsop et al., 2015), the effects of ASL were measured using a non-background suppressed 2D acquisition, which is susceptible to artifacts in the resulting CBF maps. We employed an advanced data cleaning strategy to minimize artifacts. CARDIA ASL MRI data were also acquired at a resolution of $3.4 \times 3.4x5mm^3$, which results in some partial volume effects at the voxel level, though the conclusions of this study are unlikely to be affected by this factor. Note that the ADC ASL data did not suffer from the same limitations since the background-suppressed acquisition is expected to produce less artifactual contamination (Wu et al., 2009). Moreover, the acquisition also used 2.5 mm isotropic voxels, which were previously shown to maximize the ratio between gray matter and white matter (Chang et al., 2016) and should therefore minimize partial volume effects. The ADC cohort studied using the more advanced ASL MRI acquisition strategy yielded very similar results to those seen in the CARDIA cohort.

Finally, lesion segmentations obtained using the automated LST method may not be fully accurate. However, we verified the automated segmentations by visual inspection in about 10% of subjects in each cohort and confirmed that the automated segmentations appeared accurate across subjects with varying lesion burdens.

Because the PSV ROI is in a region supplied exclusively by small vessels (Moody et al., 1990), PSV CBF provides a simple scalar value representing small vessel function that may potentially serve as a mechanistically specific biomarker of CSVD. For the ROI analyses reported in this study, we empirically defined a PSV ROI based on a CBF threshold of CBF $< 15$ ml/100 g/min, symmetrized across hemispheres. The threshold was previously shown to predict future occurrence of lesions (Bernbaum et al., 2015), albeit with CBF measured using dynamic susceptibility contrast imaging. The PSV ROI definition can be further refined in future work, ideally using longitudinal data with clinical outcomes to test the predictive value of PSV CBF for outcomes related to SVD. The optimal PSV ROI may ultimately even incorporate information from WML frequency distributions (Habes et al., 2016; Habes et al., 2018).

## 5. Conclusion

This study confirmed that the PVWM region is characterized by the lowest regional perfusion values in the brain in both middle-aged and in elderly adults, and coincides spatially with the highest white matter lesion frequencies in both cohorts. A data-driven PSV ROI defined by subthreshold CBF demonstrated a differential relationship between CBF and WML compared to the remaining white matter, suggesting that the pathophysiology of WML in the PSV ROI may be more uniformly associated with chronic hypoperfusion. While the current “gold-standard” biomarker for CSVD is WMLs, they represent downstream effects of CSVD and are not uniquely associated with ischemia, whereas PSV CBF may provide a mechanistically specific biomarker of small vessel function. Prospective evaluation of PSV CBF as a predictive biomarker of both clinical and radiographic evidence of CSVD will be the next critical step in the evaluation of this concept.

## Declaration of Competing Interests

The authors report no conflicting interests.

## Funding

CARDIA is supported by contracts HHSN268201300025C, HHSN268201300026C, HHSN268 201300027C, HHSN268201300028C, HHSN268201300029C, and HHSN268200900041C from the National Heart, Lung, and Blood Institute and the Intramural Research Program of the National Institute on Aging. This study was further supported by NIH grants R01 MH080729, P41 EB015893, R01 AG040271, P30 AG010124, R00 HD074649 and R03 AG063213.

## Acknowledgements

The authors thank Dr. Joao Lima for his insightful comments.

## Appendix A. Supplementary data

Supplementary data to this article can be found online at https://doi.org/10.1016/j.nicl.2019.101897.

## References

Alsop, D.C., Detre, J.A., Golay, X., Gunther, M., Hendrikse, J., Hernandez-Garcia, L., Lu, H., Macintosh, B.J., Parkes, L.M., Smits, M., van Osch, M.J., Wang, D.J., Wong, E.C., Zaharchuk, G., 2015. Recommended implementation of arterial spin-labeled perfusion MRI for clinical applications: a consensus of the ISMRM perfusion study group and the European consortium for ASL in dementia. Magn. Reson. Med. 73, 102–116.

Andersson, J.L.R., Jenkinson, M., Smith, S., 2010. Non-linear registration, aka spatial normalisation. In: FMRIB Technical Report TR07JA2.

Bahrani, A.A., Powell, D.K., Yu, G., Johnson, E.S., Jicha, G.A., Smith, C.D., 2017. White matter hyperintensity associations with cerebral blood flow in elderly subjects stratified by cerebrovascular risk. J. Stroke Cerebrovasc. Dis. 26, 779–786.

Bernbaum, M., Menon, B.K., Fick, G., Smith, E.E., Goyal, M., Frayne, R., Coutts, S.B., 2015. Reduced blood flow in normal white matter predicts development of leukoaraiosis. J. Cereb. Blood Flow Metab. 35, 1610–1615.

Bisschops, R.H., Van Der Graaf, Y., Mali, W.P., Van Der Grond, J., Group, S.S., 2004. High total cerebral blood flow is associated with a decrease of white matter lesions. J. Neurol. 251, 1481–1485.

Brickman, A.M., Zahra, A., Muraskin, J., Steffener, J., Holland, C.M., Habeck, C., Borogovac, A., Ramos, M.A., Brown, T.R., Asllani, I., Stern, Y., 2009. Reduction in cerebral blood flow in areas appearing as white matter hyperintensities on magnetic resonance imaging. Psychiatry Res. 172, 117–120.

Buxton, R.B., Frank, L.R., Wong, E.C., Siewert, B., Warach, S., Edelman, R.R., 1998. A general kinetic model for quantitative perfusion imaging with arterial spin labeling. Magn. Reson. Med. 40, 383–396.

Caplan, L.R., Hennerici, M., 1998. Impaired clearance of emboli (washout) is an important link between hypoperfusion, embolism, and ischemic stroke. Arch. Neurol. 55, 1475–1482.

Chang, Y.V., Vidorreta, M., Wang, Z., Detre, J.A., 2016. 3D-accelerated, stack-of-spirals acquisitions and reconstruction of arterial spin labeling MRI. Magn. Reson. Med. 78 (4), 1405–1419.

Chen, Y., Wang, D.J., Detre, J.A., 2011. Test-retest reliability of arterial spin labeling with common labeling strategies. J. Magn. Reson. Imaging 33, 940–949.

Dai, W., Garcia, D., de Bazelaire, C., Alsop, D.C., 2008. Continuous flow-driven inversion for arterial spin labeling using pulsed radio frequency and gradient fields. Magn. Reson. Med. 60, 1488–1497.

De Groot, J.C., De Leeuw, F.E., Oudkerk, M., Van Gijn, J., Hofman, A., Jolles, J., Breteler, M.M., 2002. Periventricular cerebral white matter lesions predict rate of cognitive decline. Ann. Neurol. 52, 335–341.

de Leeuw, F.E., de Groot, J.C., Oudkerk, M., Witteman, J.C., Hofman, A., van Gijn, J., Breteler, M.M., 2002. Hypertension and cerebral white matter lesions in a prospective cohort study. Brain 125, 765–772.

DeCarli, C., Fletcher, E., Ramey, V., Harvey, D., Jagust, W.J., 2005. Anatomical mapping of white matter hyperintensities (WMH): exploring the relationships between periventricular WMH, deep WMH, and total WMH burden. Stroke 36, 50–55.

Dolui, S., Wang, Z., Shinohara, R.T., Wolk, D.A., Detre, J.A., Alzheimer's Disease Neuroimaging, I, 2016a. Structural correlation-based outlier rejection (SCORE) algorithm for arterial spin labeling time series. J. Magn. Reson. Imaging 45, 1786–1797.

Dolui, S., Wang, Z., Wang, D.J., Mattay, R., Finkel, M., Elliott, M., Desiderio, L., Inglis, B., Mueller, B., Stafford, R.B., Launer, L.J., Jacobs Jr., D.R., Bryan, R.N., Detre, J.A., 2016b. Comparison of non-invasive MRI measurements of cerebral blood flow in a large multisite cohort. J. Cereb. Blood Flow Metab. 36, 1244–1256.

Dolui, S., Wolk, D.A., Detre, J.A., 2016c. SCRUB: A structural correlation and empirical robust Bayesian method for ASL data. In: Proceedings of the International Society of Magnetic Resonance in Medicine, Singapore.

Dolui, S., Vidorreta, M., Wang, Z., Nasrallah, I.M., Alavi, A., Wolk, D.A., Detre, J.A., 2017. Comparison of PASL, PCASL, and background-suppressed 3D PCASL in mild cognitive impairment. Hum. Brain Mapp. 38, 5260–5273.

Fazekas, F., Chawluk, J.B., Alavi, A., Hurtig, H.I., Zimmerman, R.A., 1987. MR signal abnormalities at 1.5 T in Alzheimer's dementia and normal aging. AJR Am. J. Roentgenol. 149, 351–356.

Fernando, M.S., Simpson, J.E., Matthews, F., Brayne, C., Lewis, C.E., Barber, R., Kalaria, R.N., Forster, G., Esteves, F., Wharton, S.B., Shaw, P.J., O'Brien, J.T., Ince, P.G., Function, M.R.C.C., Ageing Neuropathology Study, G, 2006. White matter lesions in an unselected cohort of the elderly: molecular pathology suggests origin from chronic hypoperfusion injury. Stroke 37, 1391–1398.

Ghaznawi, R., Geerlings, M.I., Jaarsma-Coes, M.G., Zwartbol, M.H., Kuijf, H.J., van der Graaf, Y., Witkamp, T.D., Hendrikse, J., de Bresser, J., Group, S.S, 2018. The association between lacunes and white matter hyperintensity features on MRI: the SMART-MR study. J. Cereb. Blood Flow Metab. https://doi.org/10.1177/0271678X18800463. (271678X18800463).

Griffanti, L., Jenkinson, M., Suri, S., Zsoldos, E., Mahmood, A., Filippini, N., Sexton, C.E., Topiwala, A., Allan, C., Kivimaki, M., Singh-Manoux, A., Ebmeier, K.P., Mackay, C.E., Zamboni, G., 2018. Classification and characterization of periventricular and deep white matter hyperintensities on MRI: a study in older adults. Neuroimage 170, 174–181.

Gunning-Dixon, F.M., Raz, N., 2003. Neuroanatomical correlates of selected executive functions in middle-aged and older adults: a prospective MRI study. Neuropsychologia 41, 1929–1941.
Habes, M., Erus, G., Toledo, J.B., Zhang, T., Bryan, N., Launer, L.J., Rosseel, Y., Janowitz, D., Doshi, J., Van der Auwera, S., von Sarnowski, B., Hegenscheid, K., Hosten, N., Homuth, G., Volzke, H., Schminke, U., Hoffmann, W., Grabe, H.J., Davatzikos, C., 2016. White matter hyperintensities and imaging patterns of brain ageing in the general population. Brain 139, 1164–1179.
Habes, M., Sotiras, A., Erus, G., Toledo, J.B., Janowitz, D., Wolk, D.A., Shou, H., Bryan, N.R., Doshi, J., Volzke, H., Schminke, U., Hoffmann, W., Resnick, S.M., Grabe, H.J., Davatzikos, C., 2018. White matter lesions: spatial heterogeneity, links to risk factors, cognition, genetics, and atrophy. Neurology 91, e964–e975.
Henriksen, O.M., Vestergaard, M.B., Lindberg, U., Aachmann-Andersen, N.J., Lisbjerg, K., Christensen, S.J., Rasmussen, P., Olsen, N.V., Forman, J.L., Larsson, H.B.W., Law, I., 2018. Interindividual and regional relationship between cerebral blood flow and glucose metabolism in the resting brain. J. Appl. Physiol. (1985) 125, 1080–1089.
Holland, C.M., Smith, E.E., Csapo, I., Gurol, M.E., Brylka, D.A., Killiany, R.J., Blacker, D., Albert, M.S., Guttmann, C.R., Greenberg, S.M., 2008. Spatial distribution of white-matter hyperintensities in Alzheimer disease, cerebral amyloid angiopathy, and healthy aging. Stroke 39, 1127–1133.
Ito, H., Inoue, K., Goto, R., Kinomura, S., Taki, Y., Okada, K., Sato, K., Sato, T., Kanno, I., Fukuda, H., 2006. Database of normal human cerebral blood flow measured by SPECT: I. comparison between I-123-IMP, Tc-99m-HMPAO, and Tc-99m-ECD as referred with O-15 labeled water PET and voxel-based morphometry. Ann. Nucl. Med. 20, 131–138.
Jenkinson, M., Beckmann, C.F., Behrens, T.E., Woolrich, M.W., Smith, S.M., 2012. FSL. Neuroimage 62, 782–790.
Jimenez-Conde, J., Biffi, A., Rahman, R., Kanakis, A., Butler, C., Sonni, S., Massasa, E., Cloonan, L., Gilson, A., Capozzo, K., Cortellini, L., Ois, A., Cuadrado-Godia, E., Rodriguez-Campello, A., Furie, K.L., Roquer, J., Rosand, J., Rost, N.S., 2010. Hyperlipidemia and reduced white matter hyperintensity volume in patients with ischemic stroke. Stroke 41, 437–442.
Kandel, B.M., Avants, B.B., Gee, J.C., McMillan, C.T., Erus, G., Doshi, J., Davatzikos, C., Wolk, D.A., 2016. White matter hyperintensities are more highly associated with preclinical Alzheimer's disease than imaging and cognitive markers of neurodegeneration. Alzheimers Dement (Amst) 4, 18–27.
Kim, K.W., MacFall, J.R., Payne, M.E., 2008. Classification of white matter lesions on magnetic resonance imaging in elderly persons. Biol. Psychiatry 64, 273–280.
Kuo, H.K., Lipsitz, L.A., 2004. Cerebral white matter changes and geriatric syndromes: is there a link? J. Gerontol. A Biol. Sci. Med. Sci. 59, 818–826.
Lee, S., Viqar, F., Zimmerman, M.E., Narkhede, A., Tosto, G., Benzinger, T.L., Marcus, D.S., Fagan, A.M., Goate, A., Fox, N.C., Cairns, N.J., Holtzman, D.M., Buckles, V., Ghetti, B., McDade, E., Martins, R.N., Saykin, A.J., Masters, C.L., Ringman, J.M., Ryan, N.S., Forster, S., Laske, C., Schofield, P.R., Sperling, R.A., Salloway, S., Correia, S., Jack Jr., C., Weiner, M., Bateman, R.J., Morris, J.C., Mayeux, R., Brickman, A.M., Dominantly Inherited Alzheimer, N, 2016. White matter hyperintensities are a core feature of Alzheimer's disease: evidence from the dominantly inherited Alzheimer network. Ann. Neurol. 79, 929–939.
Liao, D., Cooper, L., Cai, J., Toole, J.F., Bryan, N.R., Hutchinson, R.G., Tyroler, H.A., 1996. Presence and severity of cerebral white matter lesions and hypertension, its treatment, and its control. The ARIC study. Atherosclerosis risk in communities study. Stroke 27, 2262–2270.
Longstreth Jr., W.T., Manolio, T.A., Arnold, A., Burke, G.L., Bryan, N., Jungreis, C.A., Enright, P.L., O'Leary, D., Fried, L., 1996. Clinical correlates of white matter findings on cranial magnetic resonance imaging of 3301 elderly people. The cardiovascular health study. Stroke 27, 1274–1282.
Mantyla, R., Erkinjuntii, T., Salonen, O., Aronen, H.J., Peltonen, T., Pohjasvaara, T., Standertskjold-Nordenstam, C.-G., 1997. Variable agreement between visual rating scales for white matter hyperintensities on MRI: comparison of 13 rating scales in a poststroke cohort. Stroke 28, 1614–1623.
Marchant, N.L., Reed, B.R., DeCarli, C.S., Madison, C.M., Weiner, M.W., Chui, H.C., Jagust, W.J., 2012. Cerebrovascular disease, beta-amyloid, and cognition in aging. Neurobiol. Aging 33 (1006), e1025–e1036.
Mayda, A.B., Westphal, A., Carter, C.S., DeCarli, C., 2011. Late life cognitive control deficits are accentuated by white matter disease burden. Brain 134, 1673–1683.
McAleese, K.E., Walker, L., Graham, S., Moya, E.L.J., Johnson, M., Erskine, D., Colloby, S.J., Dey, M., Martin-Ruiz, C., Taylor, J.P., Thomas, A.J., McKeith, I.G., De Carli, C., Attems, J., 2017. Parietal white matter lesions in Alzheimer's disease are associated with cortical neurodegenerative pathology, but not with small vessel disease. Acta Neuropathol. 134, 459–473.
Moody, D.M., Bell, M.A., Challa, V.R., 1990. Features of the cerebral vascular pattern that predict vulnerability to perfusion or oxygenation deficiency: an anatomic study. AJNR 11, 431–439.
O'Sullivan, M., Lythgoe, D.J., Pereira, A.C., Summers, P.E., Jarosz, J.M., Williams, S.C., Markus, H.S., 2002. Patterns of cerebral blood flow reduction in patients with ischemic leukoaraiosis. Neurology 59, 321–326.
Pantoni, L., 2010. Cerebral small vessel disease: from pathogenesis and clinical characteristics to therapeutic challenges. Lancet Neurol. 9, 689–701.
Pantoni, L., Garcia, J.H., 1997. Pathogenesis of leukoaraiosis: a review. Stroke 28, 652–659.
Prins, N.D., Scheltens, P., 2015. White matter hyperintensities, cognitive impairment and dementia: an update. Nat. Rev. Neurol. 11, 157–165.
Promjunyakul, N., Lahna, D., Kaye, J.A., Dodge, H.H., Erten-Lyons, D., Rooney, W.D., Silbert, L.C., 2015. Characterizing the white matter hyperintensity penumbra with cerebral blood flow measures. Neuroimage Clin. 8, 224–229.
Promjunyakul, N.O., Lahna, D.L., Kaye, J.A., Dodge, H.H., Erten-Lyons, D., Rooney, W.D., Silbert, L.C., 2016. Comparison of cerebral blood flow and structural penumbras in relation to white matter hyperintensities: a multi-modal magnetic resonance imaging study. J. Cereb. Blood Flow Metab. 36, 1528–1536.
Promjunyakul, N.O., Dodge, H.H., Lahna, D., Boespflug, E.L., Kaye, J.A., Rooney, W.D., Silbert, L.C., 2018. Baseline NAWM structural integrity and CBF predict periventricular WMH expansion over time. Neurology 90, e2119–e2126.
Rostrup, E., Gouw, A.A., Vrenken, H., van Straaten, E.C., Ropele, S., Pantoni, L., Inzitari, D., Barkhof, F., Waldemar, G., Group, L.S, 2012. The spatial distribution of age-related white matter changes as a function of vascular risk factors–results from the LADIS study. Neuroimage 60, 1597–1607.
Scheltens, P., Barkhof, F., Leys, D., Pruvo, J.P., Nauta, J.J., Vermersch, P., Steinling, M., Valk, J., 1993. A semiquantative rating scale for the assessment of signal hyperintensities on magnetic resonance imaging. J. Neurol. Sci. 114, 7–12.
Schmidt, P., Gaser, C., Arsic, M., Buck, D., Forschler, A., Berthele, A., Hoshi, M., Ilg, R., Schmid, V.J., Zimmer, C., Hemmer, B., Muhlau, M., 2012. An automated tool for detection of FLAIR-hyperintense white-matter lesions in multiple sclerosis. Neuroimage 59, 3774–3783.
Shi, Y., Thrippleton, M.J., Makin, S.D., Marshall, I., Geerlings, M.I., de Craen, A.J., van Buchem, M.A., Wardlaw, J.M., 2016. Cerebral blood flow in small vessel disease: a systematic review and meta-analysis. J. Cereb. Blood Flow Metab. 36, 1653–1667.
ten Dam, V.H., van den Heuvel, D.M., de Craen, A.J., Bollen, E.L., Murray, H.M., Westendorp, R.G., Blauw, G.J., van Buchem, M.A., 2007. Decline in total cerebral blood flow is linked with increase in periventricular but not deep white matter hyperintensities. Radiology 243, 198–203.
van Dalen, J.W., Mutsaerts, H., Nederveen, A.J., Vrenken, H., Steenwijk, M.D., Caan, M.W.A., Majoie, C., van Gool, W.A., Richard, E., 2016. White matter hyperintensity volume and cerebral perfusion in older individuals with hypertension using arterial spin-labeling. AJNR Am. J. Neuroradiol. 37, 1824–1830.
van der Veen, P.H., Muller, M., Vincken, K.L., Hendrikse, J., Mali, W.P., van der Graaf, Y., Geerlings, M.I., Group, S.S., 2015. Longitudinal relationship between cerebral small-vessel disease and cerebral blood flow: the second manifestations of arterial disease-magnetic resonance study. Stroke 46, 1233–1238.
van Gelderen, P., de Zwart, J.A., Duyn, J.H., 2008. Pittfalls of MRI measurement of white matter perfusion based on arterial spin labeling. Magn. Reson. Med. 59, 788–795.
Verhaaren, B.F., Vernooij, M.W., de Boer, R., Hofman, A., Niessen, W.J., van der Lugt, A., Ikram, M.A., 2013. High blood pressure and cerebral white matter lesion progression in the general population. Hypertension 61, 1354–1359.
Vernooij, M.W., van der Lugt, A., Ikram, M.A., Wielopolski, P.A., Vrooman, H.A., Hofman, A., Krestin, G.P., Breteler, M.M., 2008. Total cerebral blood flow and total brain perfusion in the general population: the Rotterdam Scan Study. J. Cereb. Blood Flow Metab. 28, 412–419.
Vidorreta, M., Wang, Z., Rodriguez, I., Pastor, M.A., Detre, J.A., Fernandez-Seara, M.A., 2013. Comparison of 2D and 3D single-shot ASL perfusion fMRI sequences. Neuroimage 66C, 662–671.
Vidorreta, M., Wang, Z., Chang, Y.V., Wolk, D.A., Fernandez-Seara, M.A., Detre, J.A., 2017a. Whole-brain background-suppressed pCASL MRI with 1D-accelerated 3D RARE stack-of-spirals readout. PLoS One 12, e0183762.
Vidorreta, M., Zhao, L., Shankar, S., Wolf, D.H., Alsop, D.C., Detre, J.A., 2017b. In-vivo evaluation of PCASL labeling scheme and position. In: Proceedings of the International Society of Magnetic Resonance in Medicine, Honolulu, USA.
Wang, Z., 2012. Improving cerebral blood flow quantification for arterial spin labeled perfusion MRI by removing residual motion artifacts and global signal fluctuations. Magn. Reson. Imaging 30, 1409–1415.
Wardlaw, J.M., Smith, E.E., Biessels, G.J., Cordonnier, C., Fazekas, F., Frayne, R., Lindley, R.I., O'Brien, J.T., Barkhof, F., Benavente, O.R., Black, S.E., Brayne, C., Breteler, M., Chabriat, H., Decarli, C., de Leeuw, F.E., Doubal, F., Duering, M., Fox, N.C., Greenberg, S., Hachinski, V., Kilimann, I., Mok, V., Oostenbrugge, R., Pantoni, L., Speck, O., Stephan, B.C., Teipel, S., Viswanathan, A., Werring, D., Chen, C., Smith, C., van Buchem, M., Norrving, B., Gorelick, P.B., Dichgans, M., STandards for ReportIng Vascular changes on nEuroimaging (STRIVE v1), 2013. Neuroimaging standards for research into small vessel disease and its contribution to ageing and neurodegeneration. Lancet Neurol. 12, 822–838.
Wu, W.C., Edlow, B.L., Elliot, M.A., Wang, J., Detre, J.A., 2009. Physiological modulations in arterial spin labeling perfusion magnetic resonance imaging. IEEE Trans. Med. Imaging 28, 703–709.
Wu, W.C., Lin, S.C., Wang, D.J., Chen, K.L., Li, Y.D., 2013. Measurement of cerebral white matter perfusion using pseudocontinuous arterial spin labeling 3T magnetic resonance imaging–an experimental and theoretical investigation of feasibility. PLoS One 8, e82679.
Xie, L., Dolui, S., Das, S.R., Stockbower, G.E., Daffner, M., Rao, H., Yushkevich, P.A., Detre, J.A., Wolk, D.A., 2016. A brain stress test: cerebral perfusion during memory encoding in mild cognitive impairment. Neuroimage Clin. 11, 388–397.
Yoshita, M., Fletcher, E., Harvey, D., Ortega, M., Martinez, O., Mungas, D.M., Reed, B.R., DeCarli, C.S., 2006. Extent and distribution of white matter hyperintensities in normal aging, MCI, and AD. Neurology 67, 2192–2198.
Zhang, X., Ronen, I., Kan, H.E., Teeuwisse, W.M., van Osch, M.J., 2016. Time-efficient measurement of multi-phase arterial spin labeling MR signal in white matter. NMR Biomed. 29, 1519–1525.
Zhao, L., Vidorreta, M., Soman, S., Detre, J.A., Alsop, D.C., 2017. Improving the robustness of pseudo-continuous arterial spin labeling to off-resonance and pulsatile flow velocity. Magn. Reson. Med. 78, 1342–1351.